



Alkali silica reaction in concrete - Revealing the expansion mechanism by surface force measurements

Andreas Leemann^{a,b,*}, Michał Góra^{c,d}, Barbara Lothenbach^{a,e}, Manfred Heuberger^{c,d}

^a Laboratory for Concrete & Asphalt, Swiss Federal Laboratories for Materials Science and Technology (Empa), 8600 Dübendorf, Switzerland

^b School of Geography and Environmental Sciences, Ulster University, Coleraine, UK

^c Laboratory of Advanced Fibers, Swiss Federal Laboratories for Materials Science and Technology (Empa), 9014 St. Gallen, Switzerland

^d ETH Zürich, Department of Materials, 8092 Zürich, Switzerland

^e Department of Structural Engineering, Norwegian University of Science and Technology (NTNU), Trondheim, Norway

ARTICLE INFO

Keywords:

Concrete

Alkali-silica reaction

Polynuclear silica

Surface forces

Solidification pressure

ABSTRACT

Alkali-silica reaction (ASR) is a major cause for concrete deterioration worldwide. However, the mechanism leading to cracking has not been identified yet. In this study, the extended Surface Force Apparatus (eSFA) has been used to determine the surface forces of alkali-silica solutions between two atomically smooth mica surfaces. The setup imitates the situation present in reactive concrete aggregates with negatively charged silicate surfaces and negatively charged polynuclear silica in solution. The distance of strong electrostatic repulsion increases with increasing concentration of dissolved silica, leading to the buildup of pressure up to 6 MPa. When the precipitation of ASR products in confined conditions is triggered by the addition of CaCl_2 to the alkali-silica solution, the resulting solidification pressure forces the mica platelets apart and reaches 6–13 MPa. The eSFA experiments shows that solidification pressure is the mechanism leading to aggregate cracking and expansion of ASR-affected concrete.

1. Introduction

The alkali-silica-reaction (ASR) is a physio-chemical reaction causing severe deterioration of concrete structures worldwide [1–3]. ASR was first identified and described in detail in 1942 [4]. Despite being in the focus of concrete research since decades, the underlying mechanisms leading to stress and cracking are still under debate.

In brief, the highly alkaline pore solution present in moist concrete can lead to SiO_2 dissolution in reactive aggregate particles and to the formation of an alkali silica sol within reactive aggregates followed by the precipitation of ASR products composed of sodium, potassium, calcium, silicon, oxygen and hydrogen [5–12]. This process generates pressure and eventually leads to crack formation in the concrete.

A major difficulty in studying ASR is the identification of the first ASR products in the pre-cracking state of the concrete, due to the small quantities precipitated in pre-existing cavities of the aggregates (with dimensions from nano- to micrometers) [13,14]. The addition of caesium to concrete during production and its incorporation in ASR products increases their back-scattering contrast in the scanning

electron microscope (SEM) allowing an easy product identification, even in nanometer-sized cavities without altering the reaction [15,16]. As such, the sequence of reaction can be followed coherently. The first ASR products are formed within pre-existing voids in the aggregates at a distance of a few micrometers to tens of micrometers to the interface with the cement paste (Fig. 1a and b). With ongoing reaction, the precipitation of ASR products continuously proceeds towards the interior of the aggregate (Fig. 1c). The progressing precipitation of ASR products within the aggregates is linked to pressure formation leading to cracking (Fig. 1d).

There is a gradient in the composition of the ASR products along this pathway of precipitation, as the Ca/Si-ratio decreases with increasing distance from the interface with the cement paste. After the initial stages of the reaction, the Ca/Si-ratio and the $(\text{Na} + \text{K})/\text{Si}$ -ratio of ASR products are typically in the range of 0.25 [8,18–21]. On the other hand, the Ca/Si-ratio of the initially formed products at the front of this inward progressing precipitation (Fig. 1) can be as low as 0.05 [15,22]. Although calcium is a major component in cement hydrates, its solubility in the alkaline pore solution is relatively low due to the high pH

* Corresponding author at: Laboratory for Concrete & Asphalt, Swiss Federal Laboratories for Materials Science and Technology (Empa), 8600 Dübendorf, Switzerland.

E-mail address: andreas.leemann@empa.ch (A. Leemann).

<https://doi.org/10.1016/j.cemconres.2023.107392>

Received 20 September 2023; Received in revised form 11 November 2023; Accepted 24 November 2023

Available online 1 December 2023

0008-8846/© 2023 The Authors. Published by Elsevier Ltd. This is an open access article under the CC BY license (<http://creativecommons.org/licenses/by/4.0/>).

values [23]. However, calcium is a governing factor for the precipitation of ASR products. When added to an alkali-silica solution, calcium leads to supersaturation and precipitation [24–30]. The importance of calcium is underlined by the lack of typical ASR products and expansion in mortars and concrete with strongly dissolved reactive aggregates but an absence of calcium in the form of portlandite in the cement paste [31,32]. The width of such cracks caused by ASR ranges from a few micrometers up to dozens of micrometers [7,10,11,33,34]. Wider cracks typically propagate into the cement paste and provide a pathway for the highly concentrated alkali-silica solution present in the aggregates to diffuse into the cement paste where the concentration of the dissolved SiO_2 is low [23,35–38]. The abundance of calcium in the cement paste leads to a fast precipitation of products either close to the interface with the aggregates or along the newly formed cracks. As ASR products take up calcium and release alkalis [11,19,39–43], the final products present in the nearby cement paste are low Ca/Si-ratio types of C-S-H. The process from cracking of the aggregates, formation of low Ca/Si-ratio C-S-H along the cracks and stepwise widening of cracks is shown with its special-temporal evolution in [33,34]. The initial ASR products formed in the uncracked aggregate particles are usually amorphous [21], although different crystalline ASR products can be formed along with amorphous ones in the post-cracking state [13,18,21,44–47]. While significant progress has been made in the characterization of ASR products and the effects of ASR on concrete, the mechanisms generating stress are not clearly identified yet. So far, pressure generation and expansion have been attributed to two different processes.

- The most often postulated process is water uptake by the ASR products after their formation, resulting in swelling [48–52]. It has been proposed that the mechanism for water uptake is osmosis [53–61]. However, effective expansive stresses from observations on concrete structures and obtained by swelling gels in the laboratory are significantly smaller than the ones derived from osmotic theory [61]. Moreover, it was concluded from various tests restricting or allowing water uptake by concrete specimens expanding due to ASR, that both water imbibition by the ASR products and osmosis cannot be the major cause for expansion [62,63]. In addition, detailed investigations of synthetic and natural ASR products at different humidity levels have shown that no swelling occurs above 35 % relative humidity and that the water uptake of ASR products was significantly smaller than that of calcium-silicate-hydrate (C-S-H), the main product of cement hydration [46,47,64]. This makes the swelling of ASR products by imbibition of water an improbable cause for macroscopic expansions.
- The second proposed process is the generation of pressure by ASR products directly during their formation within the aggregates. Generation of pressure has been attributed to different mechanisms.

- It has been suggested that the doubling of the volume from (dissolved) silica in the aggregates to the precipitated ASR products in confinement causes expansion [65–68]. However, no details about the driving force of expansion are provided.
- Although scientifically not yet well explored, expansion could be attributed to crystallization pressure caused by the formation of ASR products within water containing small pores and narrow cracks. Crystallization pressure is an accepted mechanism for expansion of stones and concrete in the case of salt crystallization and sulfate attack, where it is generally related to the high degree of oversaturation of the precipitating solid [69–75]. Recent studies suggest that there is a strong link between confined mineral growth and occurrence of pressure caused by repulsive forces between negatively charged solids in the range of several MPa [76,77]. As silica surfaces become increasingly negatively charged with increasing pH [78] it can be assumed, that the presence of both negatively charged silica surface and precipitated ASR products, which also have negative surface charge at pH values >10 [79] results in considerable repulsive forces.
- The expansion due to ASR product formation has also been assigned to electrostatic repulsion caused by overlapping double layers after the precipitation of amorphous ASR products, for which a pressure in the range of 2 to 10 MPa was estimated [80–82]. The thickness of such double layers is below 1 nm and decreases with increasing ionic strength [83]. Expansive pressure calculated from surface charges of silica gel exposed to alkaline solutions indirectly determined by potentiometric titrations indicate that an expansive pressure of about 11 MPa at pH 10 can be expected [82] as illustrated in Fig. 2. However, the experimental results have been translated into a model requiring significant changes in moisture level or a strong moisture gradient in the concrete in order to cause expansion. None of the two situations is usually present in ASR affected concrete structures or concrete exposed to accelerated laboratory tests.

Surface forces play an important role in the development of crystallization pressure and electrostatic repulsion. They are crucial in understanding the interactions between solid surfaces and their surrounding environments. Direct force measurement techniques, such as atomic force microscopy (AFM) [84,85], colloidal probe microscopy (CPM) [86,87], and the surface forces apparatus (SFA) [88–91], provide valuable methodologies for the investigation of such surface forces. The SFA is a sensitive instrument designed to measure surface forces between two atomically smooth mica surfaces immersed in different liquids confined to micrometer or nanometer dimension. By employing Multiple Beam Interferometry (MBI) [88], a precise optical measurement technique, the distance between these surfaces can be measured

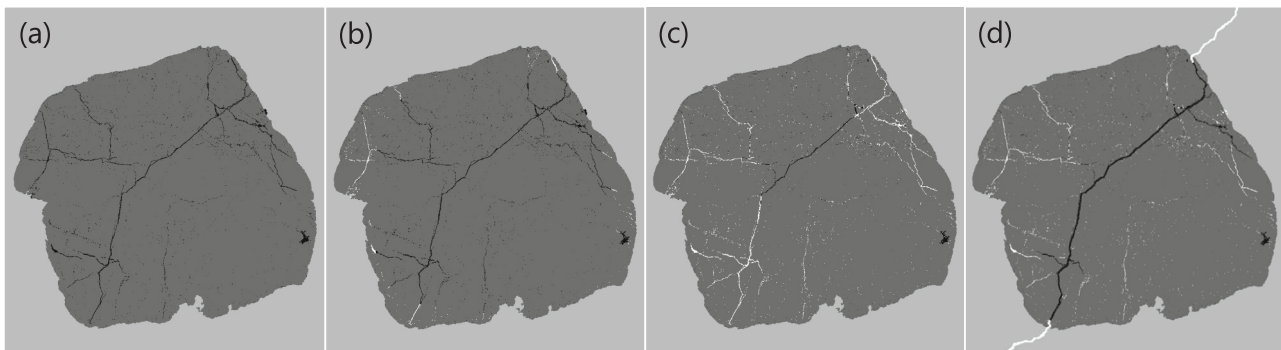


Fig. 1. Illustrative sequence of ASR with an aggregate particle (dark grey) embedded in the cement paste (light grey) of a concrete: (a) aggregate particle with pre-existing micro-cracks, (b) precipitation of ASR products (white) starting close to the interface with the cement paste, (c) continuous precipitation towards the interior of the aggregate particle and (d) cracking of aggregate and adjacent cement paste with the diffusion of alkali-silica solution into the cement paste and its precipitation along the crack. Based on data from [15] and adapted from [17].

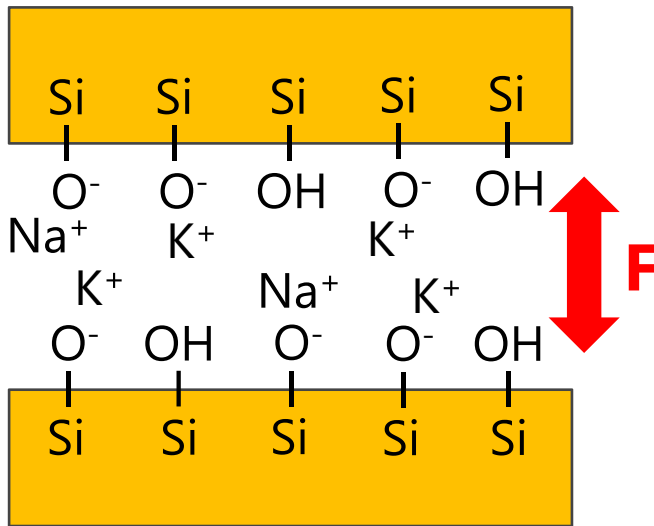


Fig. 2. Electrostatic repulsion between two negatively charged silica surfaces, which have been suggested to exert pressures up to 11 MPa at pH 10 [82].

with a resolution around 20 pm [92,93]. Such experimental configuration enables the precise assessment of surface forces occurring at various separation distances between the mica discs submerged, for example, in alkaline solutions containing varying concentrations of dissolved SiO_2 .

The experimental design of the SFA enables access to surface forces at different time scales, facilitating the investigation of dynamic systems. Additionally, the SFA setup, with its larger contact area compared to other mentioned direct force measurement techniques, provides a valuable statistical analysis of the existing surface forces in a 10–20 μm diameter nano-slit pore. In recent years, notable progress has been made in hardware and software aspects of the SFA [92,94]. These advancements led to the development of the extended Surface Force Apparatus (eSFA), which is employed as the major experimental method in this study.

Due to their possible major role in expansion caused directly by the precipitation of ASR products, the present paper aims at determining the surface forces in the presence of (polynuclear) silica dissolved in alkaline solutions. Hereby, the negatively charged mica platelets used in the eSFA can be regarded as a proxy for the negatively charged surfaces of reactive silica in concrete aggregates. Solutions with various concentrations of SiO_2 are investigated with the eSFA for three distinct scenarios:

Scenario A: Effect of an increasing SiO_2 concentration in alkaline solutions.

Scenario B: Effect of precipitated products on the mica surfaces during repeated surface approaches.

Scenario C: Effect of the precipitation of ASR products caused by the addition of CaCl_2 to the alkaline solution.

Situation A mimics the increasing SiO_2 concentration within a reactive aggregate particle during dissolution. Situation B mirrors the continuous growth of products from two opposite crack walls to the point of closure. The diffusion of calcium from the cement paste into the reactive aggregate triggering supersaturation and the precipitation of ASR products is imitated in Scenario C.

Before the eSFA experiments were executed, the mica platelets were exposed to three different alkaline solutions with a maximum pH 13.4 to study their stability in the alkaline environment. Subsequently they were investigated with the scanning electron microscope (SEM) and the atomic force microscope (AFM) to identify surface defects and their dissolution limit.

2. Materials and methods

2.1. Materials

The solutions used for assessing the chemical stability of the mica platelets were produced based on an alkaline solution, S0.4, with a total $\text{NaOH} + \text{KOH}$ concentration of 0.40 M and a pH of 13.4 (Table 1). Distilled water was added to different batches of solution S0.4 to reach pH values of 11 and 9, respectively. The pH value was measured with a Titrando 905 device with the corresponding pH-electrode (Metrohm, Switzerland). The solutions used for the surface force measurement are shown in Table 1. The alkaline solutions were produced with NaOH (Fluka 71,692) and KOH pellets (Sigma Aldrich 221,473) and with different concentrations of dissolved SiO_2 (Sigma Aldrich 833,340). The ratio between K and Na is based on the average value for Swiss cements. KNO_3 (Merck 1.05063.1000) was used for producing non-alkaline reference solutions. The CaCl_2 solution (Sigma Aldrich 1,003,161,306) to be added during the experiment exploring scenario C had a concentration of 2.3 mmol/l. This concentration was chosen as it is in the same range as the calcium concentration in the pore solution of cement pastes and mortars at an age > 2 weeks with typical values of 1–3 mmol/l [23,36]. Additionally, it allowed to reach a molar Ca/Si-ratio of 0.14 in the solution that is in the range of ASR products at an early stage of the reaction [15–17,21].

As a model substrate, ruby muscovite mica (further referred to as mica) was employed in this study. Mica substrates possess the advantageous characteristic of cleavage into atomically smooth sheets, thereby minimizing the impact of surface roughness on measurements. Additionally, mica can be cleaved into micrometer-thin sheets that exhibit adequate transparency for conducting precise eSFA experiments. A comprehensive overview of the physical and chemical properties of mica can be found in [95]. The blocks of mica (purchased from S&J Trading, USA), which were used both for assessing their stability in alkaline solution and for the surface force measurements, have a typical size of 10 mm \times 10 mm and a thickness in the range of 2–7 μm .

Samples of a concrete doped with CsNO_3 were used to help visualize the different scenarios investigated by eSFA. The concrete was subjected to an accelerated test protocol (concrete prism test conducted at 60 $^\circ\text{C}$ according to [96]) and investigated at an age of 4 weeks. Specifics of the mix design and sample preparation are given in [15].

2.2. Methods

2.2.1. Thermodynamic modelling

The Gibbs Energy Minimization software (GEMS-PSI) [97] was used to calculate the solution composition and the expected pH values. The built-in GEMS-PSI database [98] was completed with thermodynamic data describing polynuclear silica species from Felmy et al. [99], which includes dimers: $\text{Si}_2\text{O}_2(\text{OH})_5^-$, $\text{Si}_2\text{O}_3(\text{OH})_4^{2-}$, trimers: cyclic $\text{Si}_3\text{O}_6(\text{OH})_3^{3-}$, linear $\text{Si}_3\text{O}_5(\text{OH})_3^{3-}$, tetramers: cyclic $\text{Si}_4\text{O}_8(\text{OH})_4^{4-}$, substituted $\text{Si}_4\text{O}_8(\text{OH})_4^{4-}$, cyclic $\text{Si}_4\text{O}_6(\text{OH})_6^{2-}$, linear $\text{Si}_4\text{O}_7(\text{OH})_6^{4-}$ as well as hexamers: prismatic $\text{Si}_6\text{O}_{15}^{6-}$. It should be noted that potentially also octameric silicates could form [100] and that the thermodynamic data available describe aqueous silica complexes at high pH values and high silica concentrations only poorly and often underestimate the silica solubility at pH values above 12 [99,100]. The formation of quartz and amorphous SiO_2 was suppressed during the calculations of solution composition.

2.2.2. eSFA measurement technique

The extended surfaces force apparatus (eSFA) is an instrument used in surface science research for the investigation of interactions between surfaces and thin films [88,92,101]. The main purpose of the eSFA is the measurement of forces occurring between two curved surfaces that are submerged in a certain medium. The symmetric probing surface setup consists of two homogeneous and identically thick sheets of mica,

Table 1

Composition of the different solutions and calculated pH values. The Si-complexes in the different solutions are calculated with GEMS (see paragraph 3.1).

Sample	Composition [mol/L]	pH at 25 °C [–] ^a	Si species [%] ^a				
			monomer	dimer	trimer	tetramer	hexamer
R0.4	0.40 KNO ₃	7.0	–	–	–	–	–
R0.8	0.80 KNO ₃	7.0	–	–	–	–	–
S0.4	0.08 NaOH + 0.32 KOH	13.4	–	–	–	–	–
S0.4–0.2	0.08 NaOH + 0.32 KOH + 0.2 SiO ₂	12.9	62	11	9	18	<1
S0.4–0.4	0.08 NaOH + 0.32 KOH + 0.4 SiO ₂	11.2	6	12	14	56	2
S0.4–0.6 ^b	0.08 NaOH + 0.32 KOH + 0.6 SiO ₂	10.0	13	15	6	66	<1
S0.8	0.16 NaOH + 0.64 KOH	13.7	–	–	–	–	–
S0.8–0.4	0.16 NaOH + 0.64 KOH + 0.4 SiO ₂	13.2	92	3	2	3	<1
S0.8–0.8	0.16 NaOH + 0.64 KOH + 0.8 SiO ₂	10.1	53	6	8	31	2
S0.8–1.2 ^b	0.16 NaOH + 0.64 KOH + 1.2 SiO ₂	9.7	6	8	8	67	11

^a pH values and aqueous silica speciation SiO₂ predicted by thermodynamic modelling.^b Formation of amorphous SiO₂ possible based on thermodynamic calculations, but not observed in the prepared solutions.

decorated by an evaporated thin layer of silver (thickness 40 nm) on the outer side (Fig. 3). The mica sheets are glued with the silver side down on silica discs (radius ≈ 20 mm) with a thin (≈ 50 μ m) layer of thermoplastic resin glue (Shell F1004) and thus support-bent into the cylindrical shape. The cylinder axis are crossed at an angle of 90° and the lower sample is elastically suspended via a double-cantilever spring, while the upper sample is fixed to the upper frame. By moving the motor by the amount M, the distance D between the surfaces can be varied. During actuator action, the distance D is optically measured using Multiple Beam Interferometry (MBI), thus allowing to calculate the sum surface force $F = k \cdot (M - D)$; where k is the spring constant (here $k = 1450 \pm 50$ N/m), M the actuator position and D the optical measured distance. The measurement of the distance utilizing MBI involves a series of colored interference fringes transmitted upon white light illumination. The peak-wavelengths of these so-called fringes of equal chromatic order (FECO) carry the information of optical path in the interferometer [93]. The data acquisition software (Fast Spectral Correlation FSC V5, written in Labview 21) was used to process the detected interference spectra in real-time.

The wavelength calibration of the spectrometer/CCD was conducted using an Hg (Ar) lamp (ARC MS416, USA). Prior to each measurement, the CCD's dark noise characteristics were recorded, along with the acquisition of white light spectrum, ensuring the accuracy and reliability of the peak-wavelength determination for subsequent experiments.

During the actual experiments the surface forces across various alkali silica solutions, as outlined in Table 1, were investigated. This was achieved by insertion of five individual droplets, each approximately 0.1 ml in volume, of the respective alkali silica solutions between two mica sheets. In order to protect the bottom surface of the experimental instrument, a thin water film (approximately 10 ml deionized water) was applied. This water film did not come into direct contact with the actual experimental system, but was in equilibrium with it via vapor phase to keep constant relative humidity during the experiments. The

relative humidity in the experimental environment was quantified by a Sensirion SHT31 (Stäfa, Switzerland) humidity and temperature sensor. For a reference measurement the sensor was positioned at the later position of the sample surfaces. The real-time relative humidity was continuously monitored and recorded throughout a 90-min period subsequent to the vessel closing, resulting in a humidity level of (91 ± 5) %.

Once the surfaces and liquids were introduced, the instrument was allowed to undergo thermal stabilization for 90–120 min without any actuator action. The surface separation was continuously monitored to record instrumental drift at a nominal surface separation distance of $D \approx 3$ μ m. Following this stabilization period, isothermal surface force cycles (approach-separation) were recorded with a constant actuator speed of 1 nm/s. All measurements were conducted at a controlled temperature of (22.00 ± 0.02) °C outside the vessel.

2.2.3. Estimation of the contact area in eSFA experiments

The accurate estimation of contact area between surface discs in eSFA experiments holds significant importance in comprehending the interfacial forces exhibited by solid surfaces immersed in fluids. In conventional eSFA experiments, the normalized force (F/R) serves as a measure for the free energy, aligning with the principles outlined by the Derjaguin approximation [102]. Based on experimental determination of the contact area via a 3D scan [103], the pressure at a certain applied force was calculated using an estimated contact area between the discs. It is important to acknowledge that the contact area undergoes time-dependent changes during the experiment, resulting from the observed solidification effects in the alkali-silica solutions. The 3D contact scans were conducted for solutions S0.4–0.4 and S0.8–1.2 in scenario A and for the experiment in scenario C.

The precision (i.e. instrumental noise) of the eSFA in measuring surface separation is typically ± 20 pm. To reduce the systematic errors arising from an inaccurate interferometric definition, a multiple

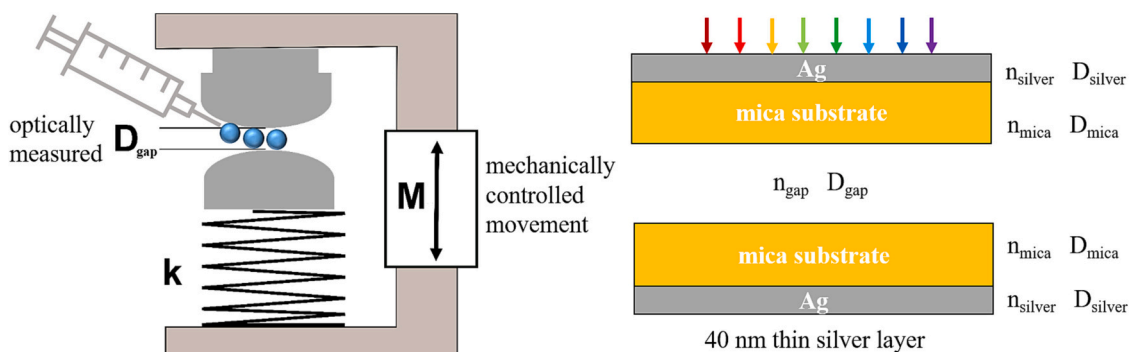


Fig. 3. Schematic representation of the Surface Forces Apparatus with the corresponding interferometer definition. Left: mechanical loop for force measurement; Right: Cross-section of thin film interferometer used as surfaces.

parameter fitting based on a 255-set spectra, recorded at different distances in dry nitrogen, was employed to extract the accurate uncompressed thickness and refractive index model of mica for each individual sample set. Typical drift rates of the eSFA (i.e. change of surface separation without actuation) after 2 h stabilization is typically <20 picometer/min. A deeper discussion of further possible systematic and statistical errors is provided in references [92, 94].

2.2.4. Scanning electron microscopy

The scanning electron micrographs to investigate the mica surface after contact with alkaline solutions were conducted on a Hitachi S-4800 Scanning Electron Microscope (SEM) operating at accelerating voltages of 20 kV in the secondary electron mode (SE). The mica sheets were coated with Au/Pd (7 nm) before analysis.

The concrete was analyzed using a scanning electron microscope (SEM) FEI Quanta 650 at a pressure of $2.5\text{--}4.0 \times 10^{-6}$ Torr. Chemical analysis was performed by energy-dispersive X-ray spectroscopy (EDS) with a Thermo Noran Ultra Dry 60mm² detector and Pathfinder X-Ray Microanalysis Software. The acceleration voltage used for imaging and EDS point analysis was 12.5 kV.

3. Results

3.1. Silica species in solution

Thermodynamic modelling indicated that the kind of Si-complexes expected in the solution depends both on the Si concentration as well as on the pH values. Below 300 mM of total Si, monomeric Si-species (mainly $(\text{SiO}_2(\text{OH})_2^-)$) dominate the solution composition, while at higher Si concentrations highly negatively charged tetrameric Si-species (mainly cyclic $\text{Si}_4\text{O}_8(\text{OH})_4^{4-}$, substituted $\text{Si}_4\text{O}_8(\text{OH})_4^{4-}$, and linear $\text{Si}_4\text{O}_7(\text{OH})_6^{4-}$) are dominant, as illustrated in Fig. 4 and summarized in Table 1. The modelling in Fig. 4 also shows that those negatively charged Si species lower the hydroxide concentrations and thus the pH values at higher SiO_2 additions. At very high SiO_2 additions, oversaturation with respect to amorphous SiO_2 gel was calculated, but not observed experimentally in (most of) the prepared solutions. This is probably due to formation of additional, stable polynuclear silica species, which are not captured in the used thermodynamic database [99,100].

3.2. Stability of mica

The mica surfaces exposed to alkaline solutions of pH 9 and 11 studied with SEM show no signs of dissolution and are identical to the untreated reference sample (Fig. 5). An increase of surface roughness is however observed in the case of the mica exposed to a highly alkaline solution of pH 13.4.

3.3. Scenario A: increasing SiO_2 concentration

The solutions S0.4 (0.4 M KOH + NaOH) and S0.8 (0.8 M KOH + NaOH) show similarly shaped onset of repulsive forces in the eSFA experiments like the two reference solutions with KNO_3 , however, with the strong repulsion occurring already at a slightly larger distance (Fig. 6). An increase in the concentration of dissolved Si in the solution S0.4–0.2, S0.4–0.4 and S0.4–0.6 leads to a corresponding increase of surface forces as shown by the increasing distance at which we record repulsion, even though a lower pH value is expected (see Table 1). Moreover, the shape of the curves changes from a sharp increase of repulsion at decreasing distance to a more continuous increase in those solutions, where polynuclear $\text{Si}_4\text{O}_8(\text{OH})_4^{4-}$ dominates (S0.4–0.4 and S0.4–0.6). The same can be observed for solutions S0.8. However, solution S0.8–1.2 shows a sharp increase again resembling the curve shape of the solutions without dissolved SiO_2 , albeit at a larger surface separation. This could indicate the formation of an additional solid phase (possibly amorphous SiO_2) at the surface of the mica during the experiment.

In a variation of the experiment, the concentration of the solution was changed outside the slit pore (i.e. under continued repulsive confinement). Starting with solution S0.4–04 the distance is decreased until the motor reaches its maximal available load. After stopping the motor, an external load of approximately 5 mN is applied and the syringe portal is opened. One droplet (~ 0.1 ml) of solution S0.4–0.6 is added to the ~ 0.5 ml of solution S0.4–04 increasing the concentration of dissolved SiO_2 from 0.40 to ~ 0.43 mmol SiO_2 in the meniscus around the contact area. After this increase of concentration in the droplet, the instrument is sealed and stabilized again; the thickness of the confined film increases against the externally applied compressive load after a short delay of 1–2 min and grows to a value of approximately 17 nm within 12 min to reach 22 nm thickness (Fig. 7), illustrating again that increasing silica concentrations increase surface forces. Due to the relatively soft spring ($k = 1450$ N/m) that presses the surfaces together,

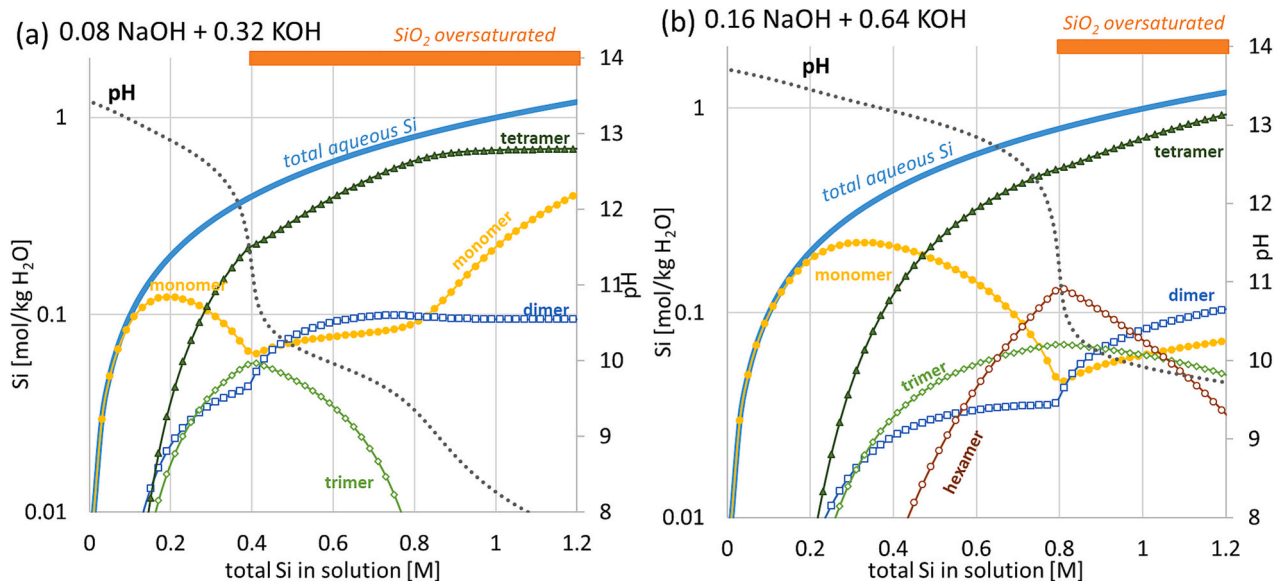


Fig. 4. Calculated Si-speciation and OH^- concentration in 0.4 (a) and 0.8 M (b) alkali (Na + K) hydroxide solution based on the thermodynamic data for polynuclear silica species from Felmy et al. [99].

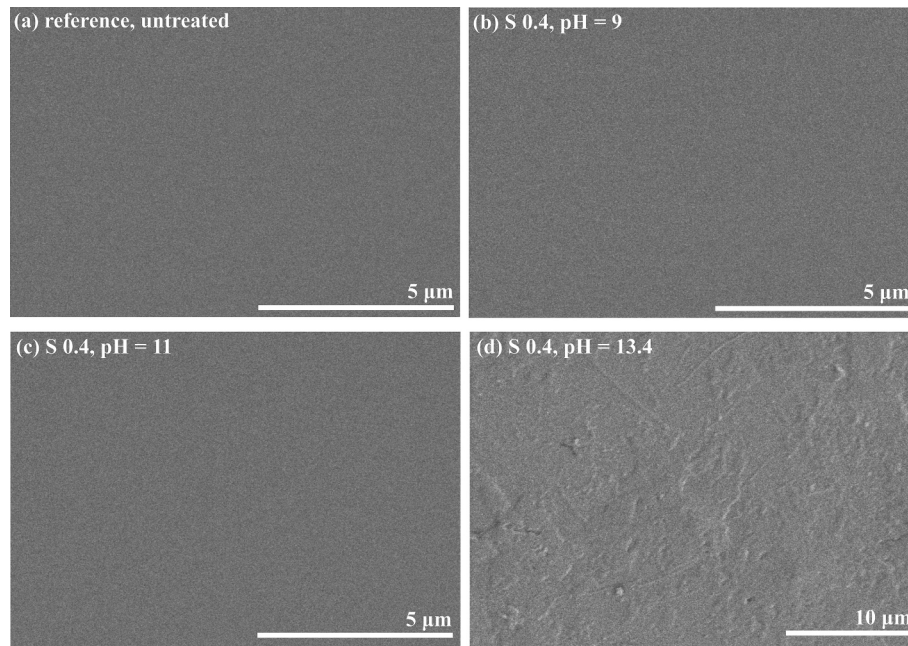


Fig. 5. SEM images of (a) reference sample without treatment, (b) mica in S 0.4 (pH = 9), (c) mica in S 0.4 (pH = 11), (d) mica in S 0.4 (pH = 13.4). Before SEM measurements, the samples were immersed in each solution for 2 h.

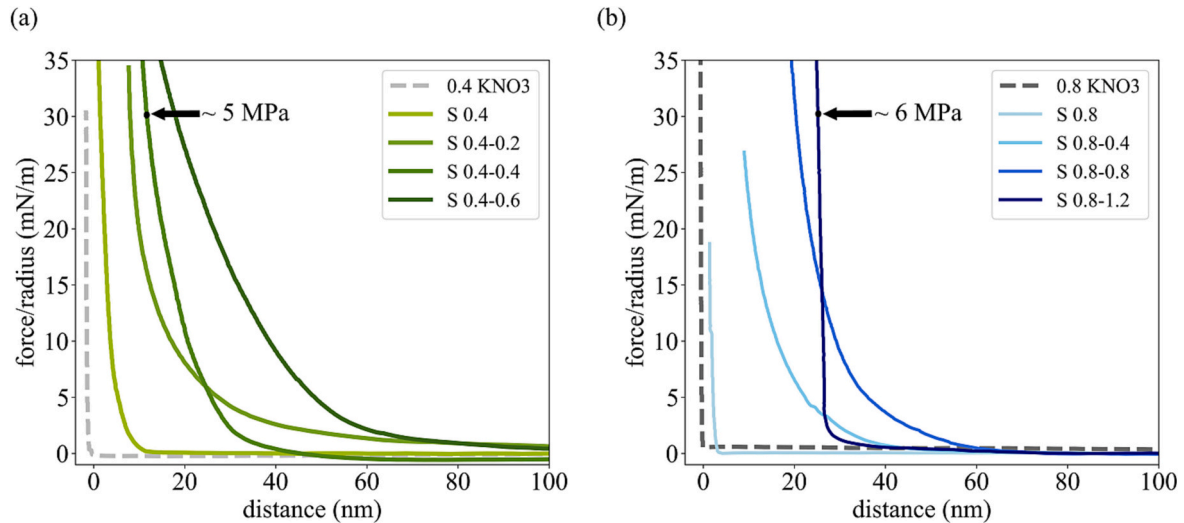


Fig. 6. Measured force/radius as a function of separation distance for the KNO_3 reference and solutions S0.4 (a) and S0.8 (b), as specified in Table 1, measured after 2 h. The arrows indicate reference locations in the curves where we quantitatively estimated confinement pressures for solutions S0.4–0.4 and S0.8–1.2 utilizing the experimentally measured contact area (i.e. contact model independent approach).

the nominal increase of external force is only 31 μN.

3.4. Scenario B: buildup of precipitated products observed upon repeated approaches

Solution S0.8–1.2 shows a sharp increase of surface forces when closing the slit pore, which is in contrast to the other solutions (Fig. 6). This may indicate the occurrence of solid surface precipitation (see paragraph 4.2), which was then further explored by repeated approaches of the mica surfaces. During the first approach, 1 h after insertion, the strong repulsion occurs at a distance of $D(F = 5 \text{ mN/m}) = 15 \text{ nm}$ (Fig. 8). Subsequently, the mica surfaces are separated to a distance of $\sim 1 \mu\text{m}$. Repeated approach separation cycles are performed. The distance of strong repulsion is continuously increasing up to $\sim 42 \text{ nm}$ in the last approach (Fig. 8). In all approaches the curve shape is the

same with a sharp increase of repulsion.

3.5. Scenario C: effect of ASR product precipitation enforced by CaCl_2 addition

In order to induce precipitation of the alkali-silica solution and to measure its effect to the surface forces, the following procedure is implemented. A first surface approach is performed using one droplet ($\sim 0.1 \text{ ml}$) of solution S04–04. The external load is increased to the instrumental maximum of $L \approx 10 \text{ mN}$. Under load, five droplets ($\sim 0.5 \text{ ml}$) of CaCl_2 solution with a concentration of 2.3 mmol/l are carefully added to the S 0.4–0.4 solution in form of a growing droplet meniscus between the muscovite mica sheets. After addition and short equilibration, the molar Ca/Si-ratio in the solution is in the range of 0.14. Shortly after droplet manipulation and resuming eSFA distance measurements, a

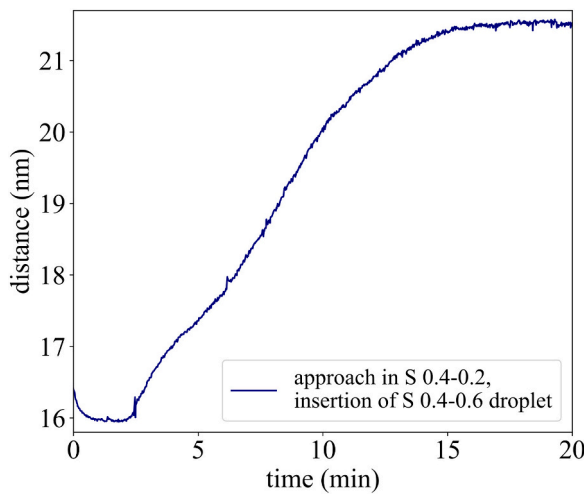


Fig. 7. Distance measurement as a function of time after increasing the SiO_2 concentration of solution S0.4–0.4 by adding solution S0.4–0.6 under confinement.

film thickness of ~ 6.5 nm is recorded (Fig. 9). The film thickness then continuously increases by an additional 16 ± 2 nm over the next 15 h up to ~ 23 nm, indicating the continued formation of a solid product. Again, the external load is constantly maintained on the slit pore. The film thickness eventually equilibrates. The same experiment is performed with a droplet of distilled water serving as a null reference of the reaction. Notably, in presence of water there is no film thickness expansion observed. Rather, the film thickness shows small isothermal fluctuations within an amplitude of ± 2 nm over a total duration of over 16 h.

From the known external force and the 3D geometry of the so formed contact area, one can readily estimate the generated pressure. Fig. 10 depicts the initial and final contact geometries, revealing considerable

deviations from a round contact in the lateral X and Y directions. The contact area was defined at a film thickness cutoff of 0.5 nm and an additional one of 1 nm above the smallest value (Fig. 10). With the known external load, the pressure can now be estimated in a contact model-independent fashion. The difference in the initial pressure and the pressure at the end of the experiment corresponds to a value of approximately 6–13 MPa at the point where the distance stabilizes after about 15 h.

3.6. Consequences for reactive concrete aggregates

Similarly to the experiments discussed above, also the formation of ASR products in concrete occurs in different situations within narrow pores in aggregate particles as illustrated in Fig. 11. The locations chosen for imaging and analysis of the concrete are exemplary for the situation of reactive but uncracked aggregate particles. Analysis of pores in the reactive quartzite, which was used as aggregate in this concrete, reveals that the cavities are mainly narrow gaps between adjacent quartz grains. In the first micrometers to tens of micrometers distance from the surface of the aggregate particles in contact with the cement paste, a low Ca/Si-ratio C-S-H is present in the pores of the aggregates, while further towards the interior of the particle, ASR product is present (Fig. 11). At this early stage of the reaction, the ASR products can extend a few hundred μm to a few mm into the reactive aggregates. However, they are expected to display a gradient in their composition with a decreasing calcium content with increasing distance from the surface of the aggregate. As the alkali content of the ASR products shows little variation [17,21] and the SiO_2 content is influenced by the quartz present in the interaction volume of the electron beam during EDS analysis, the calcium content is expressed as the molar $\text{Ca}/(\text{Na} + \text{K} + \text{Cs})$ -ratio in Fig. 12. The ASR products reaching the furthest into the aggregate display a $\text{Ca}/(\text{Na} + \text{K} + \text{Cs})$ -ratio of ~ 0.4 . This typically corresponds to molar Ca/Si -ratio of ~ 0.10 [16]. It can be expected that alkaline pore solution containing negatively charged (polynuclear) silica species dissolved from reactive SiO_2 is present in the pores not filled with ASR products. The locations corresponding to the different scenarios

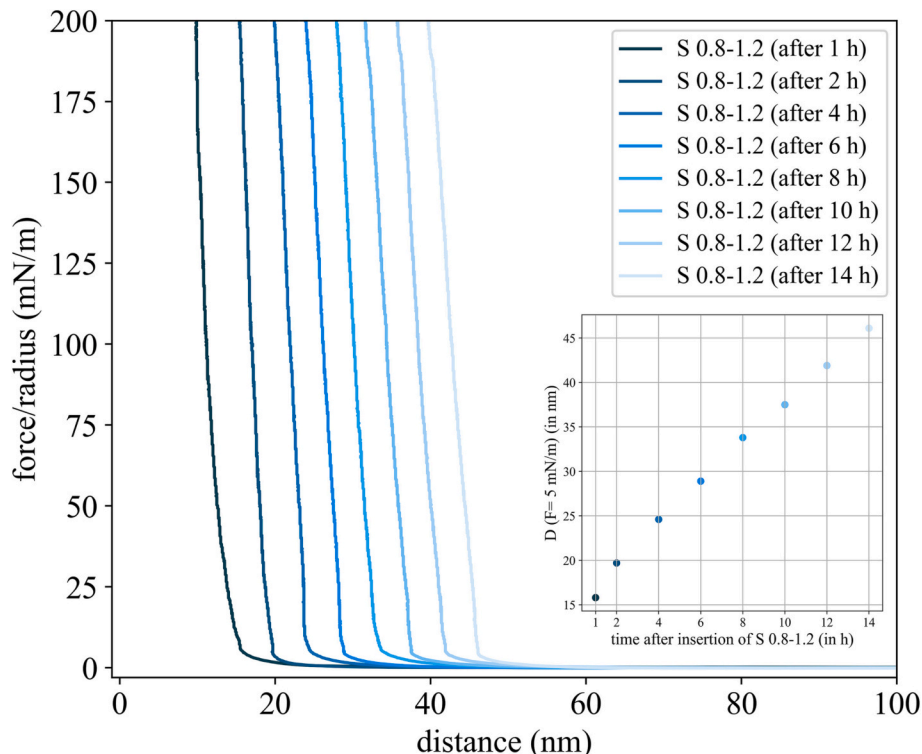


Fig. 8. Time-evolution of the measured force/radius as a function of separation distance for solution S0.8–1.2.

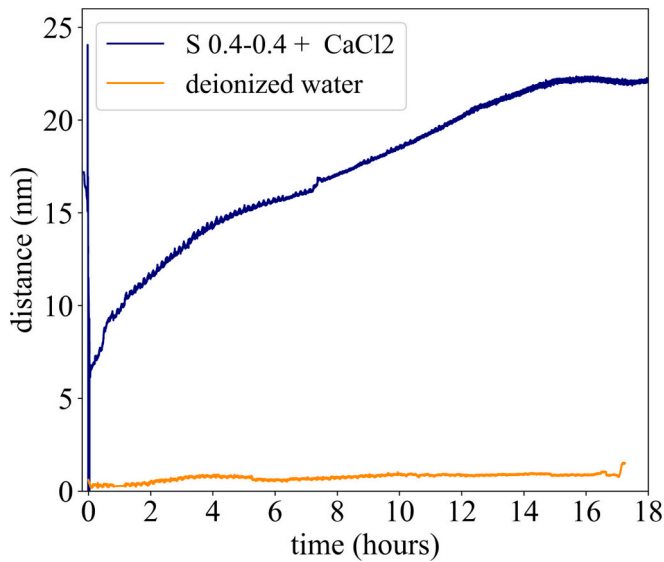


Fig. 9. Optically measured distance after insertion of CaCl_2 (blue line) or reference deionized water (orange line). (For interpretation of the references to colour in this figure legend, the reader is referred to the web version of this article.)

investigated by eSFA are indicated in Fig. 12.

The way cavities in aggregate particles are filled is evident in the case of relatively wide cracks (Fig. 13): ASR products grow from the mineral surfaces into the cavity until it is filled with products. This situation is representative for the filling of any type and size of pore or crack and is represented in scenario B in the eSFA measurements. However, there the precipitation is caused under confinement by the approaching mica surfaces. In the aggregate particles the surface of ASR products facing each other approach due to their ongoing precipitation. The surface roughness of the ASR products shown in Fig. 12 is in the range of a few hundred nm and as such considerably larger than the film thickness obtained by surface approach in the eSFA measurements, i.e. sharp increase of repulsive forces (Fig. 8). Because of these various differences, the situation as present in aggregate particles and shown in Figs. 12 and 13 was labelled with scenario B'.

4. Discussion

4.1. Stability of mica

No defects of the mica surface are observable with SEM and AFM after an exposure to alkaline solutions up to pH 11 (Fig. 5). Consequently, alterations of the mica surface and possible effects on the measurements with the solutions S0.4–0.4, S0.4–0.6, S0.8–0.8 and S0.8–1.2 can be excluded. On the other hand, the measurements with solutions S0.4 and S0.8 with a pH > 13, and possibly the ones with S0.4–0.2 and S0.8–0.4, may be affected by surface alterations of the mica caused by dissolution. When the results obtained with the two reference solutions 0.4 KNO_3 and 0.8 KNO_3 are compared to the one of S0.4 and S0.8, the measured surface forces differ. A strong repulsion is observed at a slightly greater distance in the case of solutions S0.4 and S0.8, which is attributed to the higher pH values and thus increased negatively charged mica surfaces. The differences may also partially be influenced by the increased surface roughness of the mica. A dissolution of mica would cause a smaller apparent film thickness, such that the effect of mica dissolution must thus be minor or negligible compared to the impact of pH and caused by the negatively charged dissolved silica species at pH 13.4.

4.2. Scenario A: increasing SiO_2 concentration

The increase of the SiO_2 concentration goes together with an increase in the proportion of negatively charged polynuclear silica (Table 1, Fig. 4). As a result, the distance between the mica surfaces where strong repulsion occurs is increasing with increasing concentration of (polynuclear) silica. The shape of the force curves with a “soft” continuous increase, in contrast to the steep increase of the reference solutions, suggests that there is a structural rearranging of polynuclear silica during the approach of the mica surfaces. This clearly underlines that the solutions are in a non-equilibrium condition during the approaches and gelation may occur. A steep increase of pressure similar to the reference solutions without SiO_2 is only observed in the case of solution S0.8–1.2. This strongly suggests the precipitation of a solid, most probably amorphous silica or an alkali-silicate-hydrate, on the surface of the mica. Here, it can be considered that S0.8–1.2 is saturated with respect to amorphous silica as indicated by thermodynamic modelling (Table 1, Fig. 4), as discussed further in Section 4.3.

These results can be transferred to the situation present in reactive concrete aggregates where the alkaline pore solution leads to the dissolution of SiO_2 . The repulsive forces between the aqueous negatively charged (polynuclear) silica species themselves and their interaction

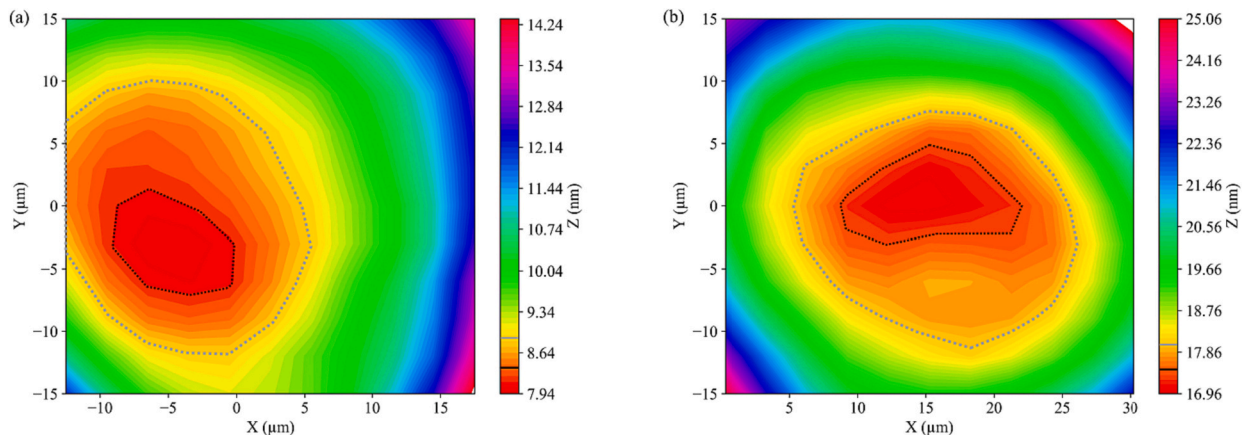


Fig. 10. 3D scans of the contact area (a) immediately after the approach in S 0.4–0.4 and insertion of CaCl_2 and (b) at the end of the measurement (after 16 h). The experimentally determined contact area (dotted line), for 0.5 nm (black) and 1 nm (grey) above the experimentally measured contact values, is used for the calculation of the pressure.

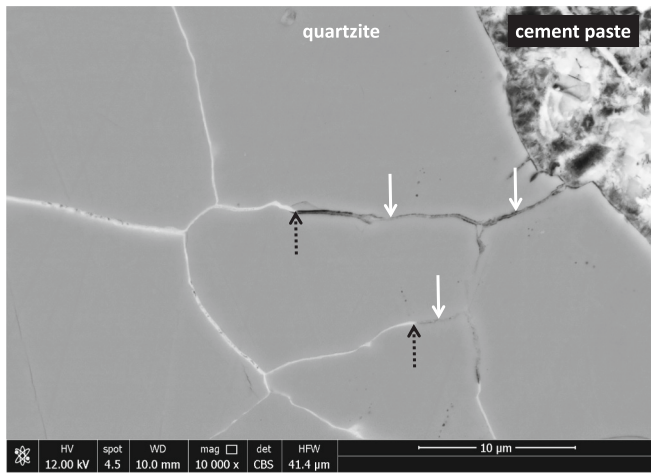


Fig. 11. Interface between an uncracked quartzite particle and the cement paste. Low Ca/Si-ratio C-S-H partly fills the cavities between adjacent quartz grains close to the interface (white arrows) and whitish ASR products containing caesium completely fill the gaps towards the interior of the quartzite particle representing scenario C (starting at the location of the dotted black arrows). The width of the original cavities between adjacent quartz grains resolved with the used magnification ranges from 20 to 350 nm. Concrete doped with CsNO_3 .

with the negatively charged surfaces of the silicate minerals in the aggregate cause electrostatic repulsion and thus pressure. This pressure increases with increasing SiO_2 concentration caused by continuous SiO_2 dissolution.

The difference between the situation in the eSFA measurements and the situation within the reactive aggregate particles in concrete are the varying parameters. In the eSFA measurements the distance between the negatively charged mica surfaces and the SiO_2 concentrations are varied, while only the SiO_2 concentration is changing within the aggregate particles. Here, the growth of the formed film against a constant compressive load in the experiment where SiO_2 concentration was increased provides a direct link to the situation in reactive aggregate particles. The fact that the mica platelets are pushed apart due to the increase of SiO_2 concentration clearly shows that a comparable increase in the pore solution of aggregate particles leads to the generation of positive pressure. In the pre-cracking state, the pressure exerted by the negatively charged silica species in the cross-section or potential

fracture plane of aggregate particles will only be present at locations where the minimum distance between negatively-charged silicate surfaces falls below 30 nm (Fig. 6). Based on microstructural observations (Fig. 11, [15]), these conditions can be expected to be met only by a certain area percentage of the cross-section. As a result, the calculated pressure of 5–6 MPa exerted by the negatively charged polynuclear silica is redistributed accordingly. For example, if the criteria of a distance <30 nm is only met by the cavities in 50 area-% of a potential fracture plane in aggregate particles, the average pressure is reduced by a factor of 2. The percentage of pores <30 nm is aggregate-specific and can exhibit large variations between different rock types [104–107].

4.3. Scenario B: effect of precipitated products during repeated approaches

The increasing distance of strong repulsion during the repeated approaches in the eSFA indicates that a layer of solid with increasing thickness is forming on the mica surfaces. The identical shape of the curves during consecutive approaches indicates that very similar surface forces are present. The precipitation of the solid in the solution S0.8–1.2 saturated with amorphous SiO_2 is likely spontaneous and not necessarily linked to the approaches. This is indicated by the differences in the

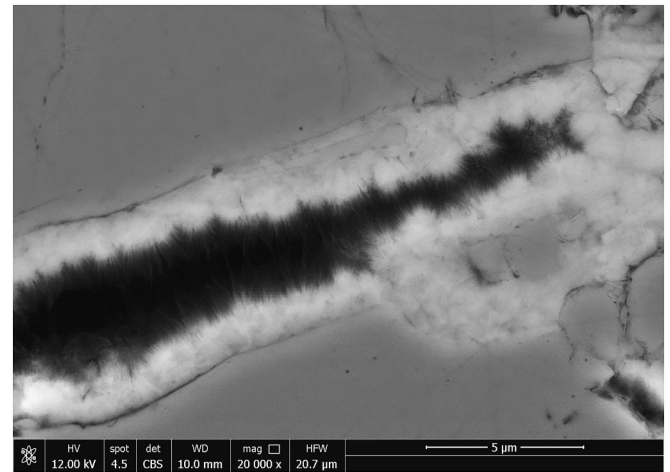


Fig. 13. ASR products starting to fill a relatively wide crack in a quartzite particle by growing from opposite crack walls, representing scenario B'.

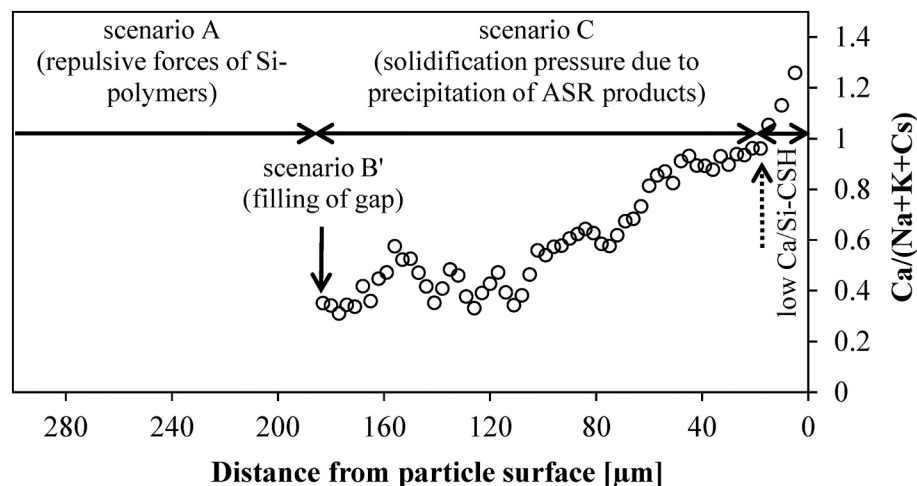


Fig. 12. Atomic $\text{Ca}/(\text{Na} + \text{K} + \text{Cs})$ -ratio of products formed in the gaps between adjacent quartz grains in the uncracked aggregate particle shown in Fig. 11 as a function of the distance to the interface with the cement paste. The dotted black arrow indicates the transition point between low Ca/Si-ratio C-S-H and ASR products. The locations where scenarios A, B' and C apply are indicated.

results with solution S0.8–1.2 in scenario A and in scenario B. The time between insertion of the solution and the approach in scenario A was two hours and in scenario B only one hour. The higher distance of strong repulsion in scenario A compared to scenario B indicates that a thicker layer of solid has formed after two hours compared to one hour.

In reactive aggregate particles, the gaps between adjacent silicate minerals differ from a few nm to several μm . Additionally, there are pores of varying shape and size. After cracking, crack width can increase to tens of μm . In such different types of cavities, ASR products typically precipitate on the surface of the minerals bordering the cavities (Fig. 13). As precipitation continuously progresses, the distance between products precipitated on the opposing sides of the cavities is decreasing until they reach the distance of repulsion ($\sim 30\text{ nm}$). When the distance of repulsion is reached, the pressure between the negatively charged dissolved silica species and the negatively charged precipitated products is generated in the same way as shown in scenario A. In regard to the surface forces at play during this process, the thickness of the two layers seem to have a negligible influence, as indicated by the eSFA measurements. The precipitated products eventually start to grow together. In the case of intergrowth, scenario C comes into effect.

4.4. Scenario C: effect of ASR product precipitation enforced by CaCl_2 addition

The addition of the Ca to an alkali-silica solution leads to supersaturation and precipitation of a solid ASR product [26–29,108]. This applies as well to solution S0.4–0.4 after the addition of CaCl_2 . The molar Ca/Si-ratio in the solution after the addition of the CaCl_2 is approximately 0.14. If the precipitated product exhibits a similar Ca/Si-ratio, it is in the range of amorphous ASR products formed in concrete [16,17,21]. Synthesized ASR products with a similar Ca/Si-ratio are dominated by Q^3 -sites (Si-tetrahedra with three bridging oxygen atoms typical for a layered Si structure) and to a lesser amount by Q^2 -sites (Si-tetrahedra with two bridging oxygen atoms typical for a chain like Si structure) [21].

The precipitation of the ASR products is linked to the direct generation of pressure that pushes the mica platelets apart in the eSFA (Fig. 9). In concrete aggregates, it is sustained by the diffusion of alkalis, calcium and silica to the precipitation sites (Figs. 11–13) and the pressure is generated by the electrostatic repulsion between the negatively charged precipitate, the negatively charged (polynuclear) silica in solution and the negatively charged aggregate surfaces, as illustrated in Fig. 14. The pressure generated by the precipitation of the non-crystalline ASR product can be described as a solidification pressure observed as repulsive forces. Consequently, pressure generation is not related to water absorption of ASR products.

The asymptotic stabilization of the distance between the mica

surfaces in scenario C after 15 h (Fig. 9) indicates that the system is close to equilibrium conditions. If it is considered that the force transmission across precipitated ASR products exhibits a certain degree of heterogeneity, one can still estimate average pressure and peak pressure within the established contact area (Fig. 10). In this context, the punctual pressure in the contact area may exceed the indicated range of 6–13 MPa for the average pressure. In any case, the solidification pressure of approximately 6–13 MPa calculated in the eSFA experiment based on the measured force and the contact areas determined by 3D scanning is equal or higher than the one exerted by polynuclear silica in solution (5–6 MPa, Fig. 6). Moreover, there is another significant difference between them. The precipitating ASR products fill cavities in reactive aggregate particles that are far wider than the ones $<30\text{ nm}$ required for pressure generation by polynuclear silica in solution (scenario A). As such, the generation of pressure is not limited to a specific cavity width. Based on this consideration the pressure caused by the negatively charged polynuclear silica has to be regarded as subsidiary to the solidification pressure between ASR product and the surrounding solid providing confinement, particularly in wider pores within concrete aggregates.

Due to the ongoing precipitation of ASR products towards the interior of the aggregate particles, the percentage of filled cavities in their cross-section or potential fracture planes is increasing. This process goes along with a continuous increase of solidification pressure that reaches its maximum when the cavities in the entire cross-section are filled. However, aggregate particles may crack before this stage is reached as described in [15].

In order to establish the link between the pressure exerted by ASR products and the consequences for the generation of cracks in aggregates and concrete, the experimental results have to be embedded into a poromechanical framework considering various effects like creep, shrinkage, cement paste elasticity, restraint and anisotropies [68,109–121].

5. Conclusions

The surface forces between mica platelets in alkaline solutions containing various concentrations of dissolved SiO_2 have been studied with an extended surface force apparatus (eSFA). Three scenarios (A–C) have been investigated and the obtained results have been projected on the situation present in reactive concrete aggregate particles. Based on the results the following conclusions can be drawn:

- Scenario A: Increasing the concentration of dissolved SiO_2 in highly alkaline solutions leads to a considerable increase of the repulsive forces between the negatively charged polynuclear silica in solution and the negatively charged mica surfaces. The resulting pressure can

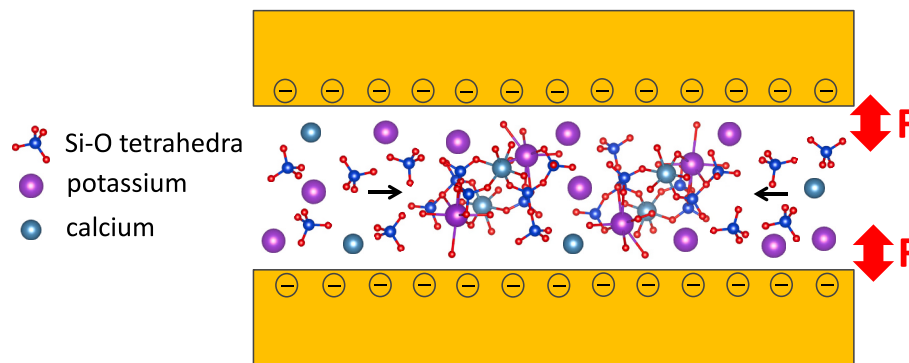


Fig. 14. Schematic illustration of the electrostatic repulsion in scenario C with the precipitation of ASR products between the mica surfaces after adding CaCl_2 . Alkalis, calcium and dissolved silica diffusing to the precipitating ASR products (black arrows) lead to the formation of more ASR products. The solidification pressure (F) between the ASR product, the negatively charged silica in solution and the negatively charged surrounding silicates widens the gap. The structure of the shown amorphous ASR product is based on K-shlykovite [64]. Sodium and hydroxide are not shown for reasons of simplification.

reach maximally up to 6 MPa, when the distance between the mica surfaces is <30 nm. As such, it can be expected that ongoing SiO₂ dissolution and increasing concentration of negatively charged polynuclear silica in reactive aggregate particles leads to comparable pressure in pores <30 nm.

- **Scenario B:** The precipitation of solid alkali-silicate-hydrates on the mica surfaces using a highly concentrated alkali-silica solution is confirmed by the increasing distance of strong repulsion during repeated approaches. The constant shape of the force curves indicates comparable repulsive surface forces with increasing thickness of the surface layers. Accordingly, the closing of cavities in aggregate particles by the growth of ASR products from the opposing mineral surfaces leads to the generation of repulsive forces by the negatively charged solids when the distance falls below approximately 30 nm.
- **Scenario C:** Forced precipitation of ASR products by adding CaCl₂ to alkali-silica solution in confined conditions leads to the formation of solid ASR products and the generation of pressure in the range of 6–13 MPa. The pressure generated by the electrostatic repulsion between the negatively charged precipitate, the negatively charged (polynuclear) silica in solution and the negatively charged mica surfaces can be regarded as solidification pressure. As such, pressure generation is not linked to water absorption of the ASR products.
- In concrete, the precipitation of ASR products towards the interior of aggregate particles increases the percentage of filled cavities in their cross-section or potential fracture planes. This process goes together with a continuous increase of the solidification pressure that may lead to the cracking of aggregate particles at any point of the progressing precipitation.
- The mechanism leading to the cracking of aggregate particles and concrete due to ASR is identified as solidification pressure exerted by precipitating negatively charged ASR products and to a lesser extent to the pressure exerted by dissolved polynuclear silica before the point of precipitation is reached.

CRediT authorship contribution statement

Andreas Leemann: Conceptualization; Formal analysis; Investigation; Methodology; Project administration; Resources; Validation; Visualization; Roles/Writing - original draft; Writing - Review & Editing.

Michal Gora: Conceptualization; Formal analysis; Investigation; Methodology; Resources; Validation; Visualization; Roles/Writing - original draft;

Barbara Lothenbach: Investigation; Methodology; Project administration; Resources; Validation; Visualization; Roles/Writing - original draft; Writing - Review & Editing.

Manfred Heuberger: Conceptualization; Funding acquisition; Methodology; Resources; Validation; Visualization; Writing - Review & Editing.

Declaration of competing interest

The authors declare the following financial interests/personal relationships which may be considered as potential competing interests: Michal Gora reports financial support was provided by Swiss National Science Foundation.

Data availability

Data will be made available on request.

Acknowledgements

The authors would like to thank Pietro Lura for suggesting to employ the extended Surface Force Apparatus to study the expansion mechanisms in ASR and for reviewing the manuscript. We acknowledge

financial support of M. Gora by the Swiss National Science Foundation (grant no. 200021_204111).

References

- [1] H. De Mayo Bernardes, N.P. Hasparyk, *Proceeding of the 15th ICAAR*, 2016.
- [2] I. Sims, A.B. Poole, *Alkali-Aggregate Reaction in Concrete: A World Review*, CRC Press, 2017.
- [3] A. Lopes Batista, A. Santos Silva, I. Fernandes, L. Oliveira Santos, J. Custódio, C. Serra, *Proceedings of the 16th ICAAR*, 2022.
- [4] T.E. Stanton, Expansion of concrete through reaction between cement and aggregate, *Trans. Am. Soc. Civ. Eng.* 107 (1942) 9–46.
- [5] S. Diamond, A review of alkali-silica reaction and expansion mechanisms 2, *Reactive aggregates, Cement and Concrete Research* 6 (1976) 549–560.
- [6] F.P. Glasser, R. Swamy, Chemistry of the alkali aggregate reaction, in: R. N. Swamy (Ed.), *The Alkali-Silica Reaction in Concrete*, Blackie, Glasgow, 1992, pp. 30–53.
- [7] B. Fournier, M.-A. Bérubé, Alkali-aggregate reaction in concrete: a review of basic concepts and engineering implications, *Can. J. Civ. Eng.* 27 (2000) 167–191.
- [8] T. Katayama, ASR gels and their crystalline phases in concrete - universal products in alkali-silica, alkali-silicate and alkali-carbonate reactions, *14th ICAAR/Austin*, 2012, pp. 20–25.
- [9] F. Rajabipour, E. Giannini, C. Dunat, J.H. Ideker, M.D.A. Thomas, Alkali-silica reaction: current understanding of the reaction mechanisms and the knowledge gaps, *Cem. Concr. Res.* 76 (2015) 130–146.
- [10] A. Leemann, T. Katayama, I. Fernandes, M.A.T.M. Broekmans, Types of alkali-aggregate reactions and the products formed, *Proceedings of the Institution of Civil Engineers - Construction Materials* 169 (2016) 128–135.
- [11] T. Katayama, *Petrographic Study of Alkali-Aggregate Reactions in Concrete*, Department of Earth and Planetary Science, University of Tokyo, Tokyo, 2012, p. 168.
- [12] T. Knudsen, N. Thaulow, Quantitative microanalyses of alkali-silica gel in concrete, *Cem. Concr. Res.* 5 (1975) 443–454.
- [13] E. Boehm-Courjault, S. Barbotin, A. Leemann, K. Scrivener, Microstructure, crystallinity and composition of alkali-silica reaction products in concrete determined by transmission electron microscopy, *Cem. Concr. Res.* 130 (2020), 105988.
- [14] E. Boehm-Courjault, A. Leemann, Characterization of ASR products by SEM and TEM, in: *16th Euroseminar on Microscopy Applied to Building Materials/Les Diablerets*, Switzerland, 2017.
- [15] A. Leemann, B. Münch, The addition of caesium to concrete with alkali-silica reaction: implications on product identification and recognition of the reaction sequence, *Cem. Concr. Res.* 120 (2019) 27–35.
- [16] A. Leemann, Impact of different added alkalis on concrete expansion due to ASR, in: A. Lopes Batista, A. Santos Silva, I. Fernandes, L. Oliveira Santos, J. Custódio, C. Serra (Eds.), *16th ICAAR/Lisbon*, 2022, pp. 129–136.
- [17] A. Leemann, Alkali silica reaction – sequence, products and possible mechanisms of expansion, in: A. Lopes Batista, A. Santos Silva, I. Fernandes, L. Oliveira Santos, J. Custódio, C. Serra (Eds.), *16th ICAAR/Lisbon*, 2022, pp. 33–52.
- [18] N. Thaulow, U.H. Jakobsen, B. Clark, Composition of alkali silica gel and ettringite in concrete railroad ties: SEM-EDX and X-ray diffraction analyses, *Cem. Concr. Res.* 26 (1996) 309–318.
- [19] M.D.A. Thomas, The role of calcium hydroxide in alkali recycling in concrete, materials science of concrete special volume on calcium hydroxide in concrete, *American Ceramic Society* (2001) 269–280.
- [20] I. Fernandes, Composition of alkali-silica reaction products at different locations within concrete structures, *Mater. Charact.* 60 (2009) 655–668.
- [21] A. Leemann, Z. Shi, J. Lindgård, Characterization of amorphous and crystalline ASR products formed in concrete aggregates, *Cem. Concr. Res.* 137 (2020), 106190.
- [22] A. Leemann, Alkali silica reaction – sequence, products and possible mechanisms of expansion, in: A. Lopes Batista, A. Santos Silva, I. Fernandes, L. Oliveira Santos, J. Custódio, C. Serra (Eds.), *16th ICAAR/Lisbon*, 2022, pp. 33–52.
- [23] B. Lothenbach, F. Winnefeld, Thermodynamic modelling of the hydration of Portland cement, *Cem. Concr. Res.* 36 (2006) 209–226.
- [24] F. Gaboriaud, D. Chaumont, A. Nonat, B. Hanquet, A. Craievich, Study of the influence of alkaline ions (Li, Na and K) on the structure of the silicate entities in silico alkaline sol and on the formation of the silico-Calco-alkaline gel, *J. Sol-Gel Sci. Technol.* 13 (1998) 353–358.
- [25] X. Hou, L.J. Struble, R.J. Kirkpatrick, Formation of ASR gel and the roles of C-S-H and portlandite, *Cem. Concr. Res.* 34 (2004) 1683–1696.
- [26] F. Gaboriaud, A. Nonat, D. Chaumont, A. Craievich, Structural model of gelation processes of a sodium silicate sol destabilized by calcium ions: combination of SAXS and rheological measurements, *J. Non Cryst. Solids* 351 (2005) 351–354.
- [27] A. Leemann, G. Le Saout, F. Winnefeld, D. Rentsch, B. Lothenbach, Alkali-Silica Reaction: the Influence of Calcium on Silica Dissolution and the Formation of Reaction Products, *J. Am. Ceram. Soc.* 94 (2011) 1243–1249.
- [28] T. Kim, J. Olek, H. Jeong, Alkali-silica reaction: kinetics of chemistry of pore solution and calcium hydroxide content in cementitious system, *Cem. Concr. Res.* 71 (2015) 36–45.
- [29] Z. Shi, B. Lothenbach, The role of calcium on the formation of alkali-silica reaction products, *Cem. Concr. Res.* 126 (2019), 105898.
- [30] L.S. Dent Glasser, N. Kataoka, On the role of calcium in the alkali-aggregate reaction, *Cem. Concr. Res.* 12 (1982) 321–331.

- [31] S. Chatterji, The role of $\text{Ca}(\text{OH})_2$ in the breakdown of Portland cement concrete due to alkali-silica reaction, *Cem. Concr. Res.* 9 (1979) 185–188.
- [32] R.F. Bleszynski, M.D.A. Thomas, Microstructural studies of alkali-silica reaction in Fly ash concrete immersed in alkaline solutions, *Adv. Cem. Bas. Mat.* 7 (1998) 66–78.
- [33] M. Shakoorioskooie, M. Griffa, A. Leemann, R. Zboray, P. Lura, Alkali-silica reaction products and cracks: X-ray micro-tomography-based analysis of their spatial-temporal evolution at a mesoscale, *Cem. Concr. Res.* 150 (2021), 106593.
- [34] M. Shakoorioskooie, M. Griffa, A. Leemann, R. Zboray, P. Lura, Quantitative analysis of the evolution of ASR products and crack networks in the context of the concrete mesostructure, *Cem. Concr. Res.* 162 (2022), 106992.
- [35] A. Leemann, B. Lothenbach, The influence of potassium–sodium ratio in cement on concrete expansion due to alkali-aggregate reaction, *Cem. Concr. Res.* 38 (2008) 1162–1168.
- [36] A. Leemann, B. Lothenbach, C. Thalmann, Influence of superplasticizers on pore solution composition and on expansion of concrete due to alkali-silica reaction, *Construct. Build Mater.* 25 (2011) 344–350.
- [37] M. Bagheri, B. Lothenbach, K. Scrivener, The effect of paste composition, aggregate mineralogy and temperature on the pore solution composition and the extent of ASR expansion, *Mater. Struct.* 55 (2022) 192.
- [38] B. Lothenbach, F. Winnefeld, C. Alder, E. Wieland, P. Lunk, Effect of temperature on the pore solution, microstructure and hydration products of Portland cement pastes, *Cem. Concr. Res.* 37 (2007) 483–491.
- [39] A. Leemann, P. Lura, E-modulus of the alkali-silica-reaction product determined by micro-indentation, *Construct. Build Mater.* 44 (2013) 221–227.
- [40] A. Leemann, Raman microscopy of alkali-silica reaction (ASR) products formed in concrete, *Cem. Concr. Res.* 102 (2017) 41–47.
- [41] M.D.A. Thomas, The role of calcium in alkali-silica reaction, in: M. Cohen, S. Mindess, J. Skalny (Eds.), *Proceedings of Sidney Diamond Symposium on Materials Science and Engineering of Concrete and Cement-Based Composite*, Materials Science of Concrete, American Ceramic Society, Westerville, OH, USA, 1998, pp. 325–335.
- [42] I. Fernandes, Role of granitic aggregates in the deterioration of a concrete dam, *Bull. Eng. Geol. Environ.* 74 (2015) 195–206.
- [43] W.C. Hansen, Studies relating to the mechanism by which the alkali-aggregate produces expansion in concrete, *Journal of the American Concrete Institute*, 15 213–227.
- [44] R. Dähn, A. Arakcheeva, P. Schaub, P. Pattison, G. Chapuis, D. Grolimund, E. Wieland, A. Leemann, Application of micro X-ray diffraction to investigate the reaction products formed by the alkali-silica reaction in concrete structures, *Cem. Concr. Res.* 79 (2016) 49–56.
- [45] G. Geng, Z. Shi, A. Leemann, C. Borca, T. Huthwelker, K. Glazyrin, I.V. Pekov, S. Churakov, B. Lothenbach, R. Dähn, E. Wieland, Atomistic structure of alkali-silica reaction products refined from X-ray diffraction and micro X-ray absorption data, *Cem. Concr. Res.* 129 (2020), 105958.
- [46] G. Geng, S. Barbotin, M. Shakoorioskooie, Z. Shi, A. Leemann, D.F. Sanchez, D. Grolimund, E. Wieland, R. Dähn, An in-situ 3D micro-XRD investigation of water uptake by alkali-silica-reaction (ASR) product, *Cem. Concr. Res.* 141 (2021), 106331.
- [47] A. Leemann, Z. Shi, M. Wyrzykowski, F. Winnefeld, Moisture stability of crystalline alkali-silica reaction products formed in concrete exposed to natural environment, *Mater. Des.* 195 (2020), 109066.
- [48] L.J. Struble, S. Diamond, Swelling properties of synthetic alkali silica gels, *J. Am. Ceram. Soc.* 64 (1981) 652–655.
- [49] S. Chatterji, A.D. Jensen, N. Thaulow, P. Christensen, Studies of alkali-silica reaction. Part 3. Mechanisms by which NaCl and $\text{Ca}(\text{OH})_2$ affect the reaction, *Cem. Concr. Res.* 16 (1986) 246–254.
- [50] M. Moranville-Resocurd, Porosity/diffusivity and alkali-silica reaction, *MRS Online Proceedings Library (OPL)* 137 (1988) 225.
- [51] R.J. Kirkpatrick, A.G. Kalinichev, X. Hou, L. Struble, Experimental and molecular dynamics modeling studies of interlayer swelling: water incorporation in kanemite and ASR gel, *Mater. Struct.* 38 (2005) 449–458.
- [52] Z.P. Bazant, A. Steffens, Mathematical model for kinetics of alkali-silica reaction in concrete, *Cem. Concr. Res.* 30 (2000) 419–428.
- [53] T.C. Powers, H.H. Steinour, An interpretation of some published researches on the alkali-aggregate reaction part 1-the chemical reactions and mechanism of expansion, *J. Proceedings* 51 (1955) 497–516.
- [54] G. Verbeck, C. Gramlich, Osmotic Studies and Hypothesis Concerning Alkali-Aggregate Reaction, *GASTM Proceedings*, 1955.
- [55] J.E. Gillott, Alkali-aggregate reactions in concrete, *Eng. Geol.* 9 (1975) 303–326.
- [56] L.S.D. Glasser, Osmotic pressure and the swelling of gels, *Cem. Concr. Res.* 9 (1979) 515–517.
- [57] A.B. Poole, Alkali-silica reactivity mechanisms of gel formation and expansion, 9th ICAARLondon, 1992, pp. 782–789.
- [58] A. Gholizadeh Vayghan, F. Rajabipour, J.L. Rosenberger, Composition–rheology relationships in alkali-silica reaction gels and the impact on the gel's deleterious behavior, *Cem. Concr. Res.* 83 (2016) 45–56.
- [59] A. Gholizadeh-Vayghan, F. Rajabipour, The influence of alkali-silica reaction (ASR) gel composition on its hydrophilic properties and free swelling in contact with water vapor, *Cem. Concr. Res.* 94 (2017) 49–58.
- [60] W.C. Hanson, Studies relating to the mechanism by which the alkali-aggregate reaction produces expansion in concrete, *J. Proceedings* 40 (1944) 213–228.
- [61] S. Diamond, ASR-another look at mechanisms, in: 8th ICAARKyoto, 1989, pp. 83–94.
- [62] C. Larive, Apports combinés de l'expérimentation et de la modélisation à la compréhension de l'alkali-réaction et de ses effets mécaniques, *Ecole nationale des ponts et chaussées*, 1997.
- [63] C. Larive, A. Laplaud, O. Coussy, The role of water in alkali-silica reaction, 11th ICAARQuébec, Canada, 2000, pp. 61–69.
- [64] Z. Shi, G. Geng, A. Leemann, B. Lothenbach, Synthesis, characterization, and water uptake property of alkali-silica reaction products, *Cem. Concr. Res.* 121 (2019) 58–71.
- [65] S. Chatterji, Chemistry of alkali-silica reaction and testing of aggregates, *Cement and Concrete Composites* 27 (2005) 788–795.
- [66] E. Garcia-Diaz, J. Riche, D. Bulteel, C. Vernet, Mechanism of damage for the alkali-silica reaction, *Cem. Concr. Res.* 36 (2006) 395–400.
- [67] T. Ichikawa, M. Miura, Modified model of alkali-silica reaction, *Cem. Concr. Res.* 37 (2007) 1291–1297.
- [68] E.R. Gallyamov, A. Leemann, B. Lothenbach, J.F. Molinari, Predicting damage in aggregates due to the volume increase of the alkali-silica reaction products, *Cem. Concr. Res.* 154 (2022), 106744.
- [69] X. Ping, J.J. Beaudoin, Mechanism of sulphate expansion I. Thermodynamic principle of crystallization pressure, *Cement and Concrete Research* 22 (1992) 631–640.
- [70] R.J. Flatt, G.W. Scherer, Thermodynamics of crystallization stresses in DEF, *Cem. Concr. Res.* 38 (2008) 325–336.
- [71] W. Kunther, B. Lothenbach, J. Skibsted, Influence of the Ca/Si ratio of the C–S–H phase on the interaction with sulfate ions and its impact on the ettringite crystallization pressure, *Cem. Concr. Res.* 69 (2015) 37–49.
- [72] G.W. Scherer, Crystallization in pores, *Cem. Concr. Res.* 29 (1999) 1347–1358.
- [73] G.W. Scherer, Stress from crystallization of salt, *Cem. Concr. Res.* 34 (2004) 1613–1624.
- [74] J. Bizzozero, C. Gosselin, K.L. Scrivener, Expansion mechanisms in calcium aluminate and sulfoaluminate systems with calcium sulfate, *Cem. Concr. Res.* 56 (2014) 190–202.
- [75] R.M. Espinosa-Marzal, G.W. Scherer, Advances in understanding damage by salt crystallization, *Acc. Chem. Res.* 43 (2010) 897–905.
- [76] J. Desarnaud, D. Bonn, N. Shahidzadeh, The pressure induced by salt crystallization in confinement, *Sci. Rep.* 6 (2016) 30856.
- [77] J. Dziadkowiec, B. Zareepolgardani, D.K. Dythe, A. Røyne, Nucleation in confinement generates long-range repulsion between rough calcite surfaces, *Sci. Rep.* 9 (2019) 8948.
- [78] L. Bousse, S. Mostarshed, B. Van Der Shoot, N.F. de Rooij, P. Gimmel, W. Göpel, Zeta potential measurements of Ta_2O_5 and SiO_2 thin films, *J. Colloid Interface Sci.* 147 (1991) 22–32.
- [79] N. Krattiger, B. Lothenbach, S.V. Churakov, Sorption and electrokinetic properties of ASR product and C-S-H: a comparative modelling study, *Cem. Concr. Res.* 146 (2021), 106491.
- [80] M. Prezzi, P.J. Monteiro, G. Sposito, The alkali-silica reaction: part I. Use of the double-layer theory to explain the behavior of reaction-product gels, *ACI Mater. J.* 94 (1997) 10–17.
- [81] M. Prezzi, P.J. Monteiro, G. Sposito, Alkali-silica reaction-part 2: the effect of chemical admixtures, *ACI Materials Journal* 95 (1998) 3–10.
- [82] F.A. Rodrigues, P.J.M. Monteiro, G. Sposito, The alkali-silica reaction: the surface charge density of silica and its effect on expansive pressure, *Cem. Concr. Res.* 29 (1999) 527–530.
- [83] K. Bohinc, V. Kralj-Iglič, A. Iglič, Thickness of electrical double layer. Effect of ion size, *Electrochimica Acta* 46 (2001) 3033–3040.
- [84] H.-J. Butt, B. Cappella, M. Kappl, Force measurements with the atomic force microscope: technique, interpretation and applications, *Surf. Sci. Rep.* 59 (2005) 1–152.
- [85] W.A. Ducker, T.J. Senden, R.M. Pashley, Direct measurement of colloidal forces using an atomic force microscope, *Nature* 353 (1991) 239–241.
- [86] M. Kappl, H.-J. Butt, The colloidal probe technique and its application to adhesion force measurements, Part. Part. Syst. Charact. 19 (2002) 129–143.
- [87] A. Karg, T. Röbler, A. Mark, P. Markus, T. Lauster, N. Helfricht, G. Papastavrou, A versatile and simple approach to electrochemical colloidal probes for direct force measurements, *Langmuir* 37 (2021) 13537–13547.
- [88] J.N. Israelachvili, Thin film studies using multiple-beam interferometry, *J. Colloid Interface Sci.* 44 (1973) 259–272.
- [89] J.N. Israelachvili, G.E. Adams, Measurement of forces between two mica surfaces in aqueous electrolyte solutions in the range 0–100 nm, *Journal of the Chemical Society, Faraday Transactions 1: Physical Chemistry in Condensed Phases* 74 (1978) 975–1001.
- [90] A. Anzalone, J. Boles, G. Greene, K. Young, J. Israelachvili, N. Alcantar, Confined fluids and their role in pressure solution, *Chem. Geol.* 230 (2006) 220–231.
- [91] K. Kristiansen, M. Valtiner, G.W. Greene, J.R. Boles, J.N. Israelachvili, Pressure solution – the importance of the electrochemical surface potentials, *Geochim. Cosmochim. Acta* 75 (2011) 6882–6892.
- [92] M. Heuberger, The extended surface forces apparatus. Part I. Fast spectral correlation interferometry, *Review of Scientific Instruments* 72 (2001) 1700–1707.
- [93] M. Heuberger, G. Luengo, J. Israelachvili, Topographic information from multiple beam interferometry in the surface forces apparatus, *Langmuir* 13 (1997) 3839–3848.
- [94] M. Heuberger, J. Vanicek, M. Zäch, The extended surface forces apparatus. II. Precision temperature control, *Rev. Sci. Instrum.* 72 (2001) 3556–3560.
- [95] T.E. Balmer, Resolving Structural and Dynamical Properties in Nano-Confined Fluids, *ETH Zurich*, 2007.

- [96] SIA262–1, Betonbau - Ergänzende Festlegungen, Schweizerischer Ingenieur- und Architektenverein, 2019.
- [97] D. Kulik, T. Wagner, S. Dmytrieva, G. Kosakowski, F. Hingerl, K. Chudnenko, U. Berner, GEM-Selektor geochemical modeling package: revised algorithm and GEMS3K numerical kernel for coupled simulation codes, *Comput. Geosci.* 17 (2013) 1–24.
- [98] T. Thoenen, W. Hummel, U. Berner, E. Curti, The PSI/Nagra Chemical Thermodynamic Database 12/07, PSI Report 14–04, Villigen PSI, Switzerland, 2014.
- [99] A.R. Felmy, H. Cho, J.R. Rustad, M.J. Mason, An aqueous thermodynamic model for polymerized silica species to high ionic strength, *J. Solution Chem.* 30 (2001) 509–525.
- [100] C.F. Weber, R.D. Hunt, Modeling alkaline silicate solutions at 25 °C, *Ind. Eng. Chem. Res.* 42 (2003) 6970–6976.
- [101] D. Tabor, R.H.S. Winterton, The direct measurement of normal and retarded van der Waals forces, *Proceedings of the Royal Society of London. A. Mathematical and Physical Sciences* 312 (1997) 435–450.
- [102] B. Deryaguin, Untersuchungen über die Reibung und Adhäsion, IV. Theorie des Anhaftens kleiner Teilchen., *Kolloid Zeitschrift* 69, 1934, pp. 155–164.
- [103] J. Israelachvili, Y. Min, M. Akbulut, A. Alig, G. Carver, W. Greene, K. Kristiansen, E. Meyer, N. Pesika, K. Rosenberg, H. Zeng, Recent advances in the surface forces apparatus (SFA) technique, *Rep. Prog. Phys.* 73 (2010), 036601.
- [104] O.A. Kayyali, Mercury intrusion porosimetry of concrete aggregates, *Mater. Struct.* 18 (1985) 259–262.
- [105] C. Dubois, P. Couchot, A.A. Calleja, E. Boeglin, A. Chambaudet, Specific mercury porosimetry for low-porosity materials, *Meas. Sci. Technol.* 9 (1998) 2016.
- [106] N. Zhang, M. He, B. Zhang, F. Qiao, H. Sheng, Q. Hu, Pore structure characteristics and permeability of deep sedimentary rocks determined by mercury intrusion porosimetry, *J. Earth Sci.* 27 (2016) 670–676.
- [107] Z. Gao, Q. Hu, Estimating permeability using median pore-throat radius obtained from mercury intrusion porosimetry, *J. Geophys. Eng.* 10 (2013), 025014.
- [108] A. Leemann, L. Lörtscher, L. Bernard, G. Le Saout, B. Lothenbach, R.M. Espinosa-Marzal, Mitigation of ASR by the use of LiNO₃—characterization of the reaction products, *Cem. Concr. Res.* 59 (2014) 73–86.
- [109] C.F. Dunant, K.L. Scrivener, Effects of uniaxial stress on alkali–silica reaction induced expansion of concrete, *Cem. Concr. Res.* 42 (2012) 567–576.
- [110] C.F. Dunant, K.L. Scrivener, Micro-mechanical modelling of alkali–silica-reaction-induced degradation using the AMIE framework, *Cem. Concr. Res.* 40 (2010) 517–525.
- [111] E. Grimal, A. Sellier, S. Multon, Y. Le Pape, E. Bourdarot, Concrete modelling for expertise of structures affected by alkali aggregate reaction, *Cem. Concr. Res.* 40 (2010) 502–507.
- [112] S. Multon, A. Sellier, M. Cyr, Chemo–mechanical modeling for prediction of alkali silica reaction (ASR) expansion, *Cem. Concr. Res.* 39 (2009) 490–500.
- [113] S.-N. Roth, P. Léger, A. Soulaïmani, Strongly coupled XFEM formulation for non-planar three-dimensional simulation of hydraulic fracturing with emphasis on concrete dams, *Comput. Methods Appl. Mech. Eng.* 363 (2020), 112899.
- [114] J. Liaudat, I. Carol, C.M. López, Model for alkali-silica reaction expansions in concrete using zero-thickness chemo-mechanical interface elements, *Int. J. Solids Struct.* 207 (2020) 145–177.
- [115] M. Pathirage, B. Zhang, M. Alnagar, G. Cusatis, Confinement and alkali-silica reaction in concrete: review and numerical investigation, *Int. J. Solids Struct.* 277–278 (2023), 112341.
- [116] S. Multon, A. Sellier, Multi-scale analysis of alkali–silica reaction (ASR): impact of alkali leaching on scale effects affecting expansion tests, *Cem. Concr. Res.* 81 (2016) 122–133.
- [117] P. Morenon, S. Multon, A. Sellier, Modelling the mechanical behaviour of concrete subjected to alkali-silica reaction (ASR) under multi-axial stress, *Cem. Concr. Res.* 158 (2022), 106823.
- [118] P. Morenon, S. Multon, A. Sellier, E. Grimal, F. Hamon, P. Kolmayer, Flexural performance of reinforced concrete beams damaged by alkali-silica reaction, *Cem. Concr. Compos.* 104 (2019), 103412.
- [119] S. Multon, F. Toutlemonde, Effect of applied stresses on alkali–silica reaction-induced expansions, *Cem. Concr. Res.* 36 (2006) 912–920.
- [120] E.R. Gallyamov, A.I. Cuba Ramos, M. Corrado, R. Reza khani, J.F. Molinari, Multi-scale modelling of concrete structures affected by alkali-silica reaction: coupling the mesoscopic damage evolution and the macroscopic concrete deterioration, *Int. J. Solids Struct.* 207 (2020) 262–278.
- [121] R. Reza khani, E. Gallyamov, J.F. Molinari, Meso-scale finite element modeling of alkali-silica-reaction, *Construct. Build Mater.* 278 (2021), 122244.